Chapter 3
Maximum Power Point Tracking Control of Wind Energy Conversion Systems

Yong Feng and Xinghuo Yu

Abstract This chapter studies the control problems in grid integration of wind energy conversion systems. Sliding-mode control technique will be used to optimize the control of wind energy conversion systems. The maximum power point tracking control algorithms for variable-speed wind energy conversion systems are presented. The grid integration of wind energy conversion systems can be optimized in terms of power delivered to the grid and providing the voltage support ancillary service at the point of common coupling. The control objective for the grid integration of wind energy conversion systems is to keep the DC-link voltage in a desirable value and the input or output power factors staying unitary. The high-order terminal sliding-mode voltage and current regulators are designed, respectively, to control the DC-link voltage and the current rapidly and exactly. The numerical simulations will be carried out to evaluate the control schemes.

Keywords DFIG-based wind power system · Voltage-oriented control (VOC) · Grid-side PWM converter · Sliding-mode control · Terminal sliding mode

Nomenclature

P_w	Input power to the wind turbine
r	Wind turbine radius
v_w	Wind speed
ρ	Air density
P_m	Mechanical power
C_p	Power coefficient

Y. Feng (✉)
Department of Electrical Engineering, Harbin Institute of Technology,
Harbin 150001, China
e-mail: yfeng@hit.edu.cn

Y. Feng · X. Yu
School of Electrical and Computer Engineering, RMIT University, Melbourne,
VIC 3001, Australia
e-mail: x.yu@rmit.edu.au

N. Luo et al. (eds.), *Wind Turbine Control and Monitoring*,
Advances in Industrial Control, DOI 10.1007/978-3-319-08413-8_3

β	Pitch angle
λ	Tip speed ratio
ω_w	Turbine angular speed
P, Q	Active and reactive power for the induction generator
i_{ds}, i_{qs}	Stator currents in d-q axes
u_{ds}, u_{qs}	Stator voltages in d-q axes
L	Inductor of the grid side filter
R	Resistance of the grid side filter
C	DC-link capacitor
i_d, i_q	d- and q-axis current components of the converter
s_d, s_q	d- and q-axis switching control signals
e_d, e_q	d- and q-axis voltage component of the three-phase supply
ω	Angular frequency of the power source
P_{ac}, P_{dc}	Active power of AC and DC sides

3.1 Introduction

Renewable energy is an important sustainable energy in the world. It comes from natural resources, such as wind, solar, rain, tides, biomass, and geothermal heat. Up to now, as an essential part of low emissions energy in a lot of countries, renewable energy has been an important to the national energy security, and played a significant role in reducing carbon emissions.

Wind energy is a large and important renewable energy source, and widely used in the world and has become a reliable and competitive means for electric power generation. Total global wind power capacity is near 198 gigawatts (GW) in 2010 [1].

Wind energy conversion system (WECS) is an apparatus for converting the kinetic energy available in the wind to mechanical energy that can be used to operate an electrical generator for producing electricity. A typical WECS includes a wind turbine, a generator, interconnection apparatus, and control systems. Generators for wind turbines generally include the following types: synchronous, permanent magnet synchronous, doubly-fed induction, and induction generators. For small-to-medium power wind turbines, permanent-magnet and squirrel-cage induction generators are often used because of their reliability and low cost. Induction, permanent magnet synchronous, and wound field synchronous generators are currently used in various high-power wind turbines [2].

A lot of control methods for WECS have been proposed in literatures. A wind speed sensorless neural network (NN) based maximum power point tracking (MPPT) control algorithm for variable-speed WECS is proposed in [3]. The power regulation of variable-speed WECS was studied in [4]. A sliding-mode control (SMC) strategy was proposed to assure the system stability and impose the ideally designed feedback control solution in spite of model uncertainties. A second-order sliding-mode control (2-SMC) scheme for a wind turbine-driven doubly-fed induction generator (DFIG) was proposed in [5]. The tasks of grid synchronization and power control were undertaken by two different algorithms, designed to command the rotor-side converter (RSC) at fixed switching frequency. Despite conventional synchronous generators, permanent magnet synchronous generators, and doubly- fed induction generators, the switched reluctance generator (SRG) can also be considered as a wind generator. In [6], a novel speed control of SRG by using adaptive neural network (ANN) controller was presented. The SRG is driven by variable-speed wind turbine and it is connected to the grid through an asymmetric half bridge converter, DC-link, and DC-AC inverter system. Among a lot of control methods, SMC offers some superior properties including fast and finite-time convergence, and high steady-state precision [7] and has been used in WECS.

This chapter describes a control strategy for wind energy integration into power network. A typical WECS and its mathematical model are analyzed. For a wind turbine to have the maximum active power extraction from the wind at any given instant, the electrical load on the generator is regulated using the MPPT method. For wind energy integration into power network, the structure of dual PWM inverter is utilized. Both the voltage and currents in the WECS are measured and control signals for both two PWM inverters are generated based on the control algorithms. An improved outer-loop control strategy is designed to control the square of the DC-link voltage.

Compared to other control methods, sliding-mode control (SMC) has many important features, such as simplicity for implementation, high robustness to external disturbances and low sensitivity to the system parameter variations [8–11]. SMC includes conventional linear sliding-mode (LSM) control and nonlinear terminal sliding-mode (TSM) control. The former are asymptotically stable, and the latter are finite-time stable. Compared to traditional LSM control, TSM control exhibits various superior properties such as fast and finite-time convergence, and smaller steady-state tracking errors [12, 13]. In the chapter TSM is used to make the error of the current and DC-link voltage reach zero in finite time. Meanwhile, high-order sliding-mode technique is utilized to eliminate the chattering phenomenon existing in sliding-mode control. The actual control signal is soften to be continuous and smooth. The TSM control strategy described in the chapter can improve the performance of the grid-side PWM converter of the wind power system.

3.2 Model of Wind Turbine

A typical WECS is shown in Fig. 3.1. It consists of a wind turbine, a gearbox, a generator, a machine-side PWM inverter, an intermediate DC circuit, a grid side PWM inverter, a transformer, and a control system. The generator may be a synchronous, permanent magnet synchronous, doubly-fed induction, or induction generator.

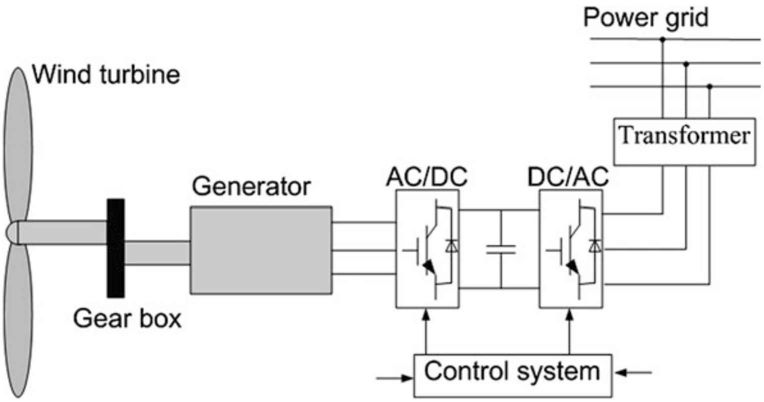

Fig. 3.1 Structure of a typical wind energy conversion system

The wind turbine absorbs the energy from an air stream and drives the generator to produce electricity. The control system is used to control both the machine side and the grid-side PWM inverters. The former controls the speed of the generator to rotate at the optimal speed and have the maximum active power extraction from the wind at different environment conditions. The latter transforms the DC voltage in the DC link to AC voltage, and further to the distribution power grid.

The input power to a wind turbine can be described as follows [3]:

$$P_w = \frac{1}{2}\rho\pi r^2 v_w^3 \tag{3.1}$$

where r is the turbine radius (m), v_w the wind speed (m/s), ρ the air density (generally it is 1.25 kg/m^3).

The mechanical power generated by the wind turbine can be expressed as follows:

$$P_m = C_p(\lambda, \beta)P_w = \frac{1}{2}C_p(\lambda, \beta)\rho\pi r^2 v_w^3 \tag{3.2}$$

where C_p is the power coefficient of the turbine representing the efficiency of the wind turbine, β the pitch angle, and λ the tip speed ratio representing the status of the turbine in different wind speeds and defined by

$$\lambda = \frac{\omega_w r}{v_w} \tag{3.3}$$

where ω_w is the turbine angular speed, as shown in Fig. 3.1.

Assume the pitch angle β is zero, the power coefficient of the turbine can be approximately expressed as follows [14, 15]:

$$C_p(\lambda, \beta) = 0.5176\left(\frac{116}{\lambda_i} - 0.4\beta - 5\right)e^{-\frac{21}{\lambda_i}} + 0.0068\lambda \tag{3.4}$$

where

$$\lambda_i = \frac{1}{\lambda + 0.08\beta} - \frac{0.035}{\beta^3 + 1}$$

To obtain the maximum active power extraction from the wind, the power coefficient Eq. (3.4) should be kept the optimal value, i.e.,

$$\left.\frac{d}{d\lambda} C_p(\lambda, \beta)\right|_{\lambda=\lambda_{opt}} = 0 \tag{3.5}$$

which can lead to $C_{pmax}(\lambda_{opt}, \beta) = \max\{C_{pmax}(\lambda, \beta)\}$ for $\lambda = \lambda_{opt}$.

The optimal maximum output power and torque of a turbine can be obtained, respectively, as follows from Eqs. (3.2), (3.3) and (3.5):

$$P_{m\max} = K_{opt}\omega_{wopt}^3 \tag{3.6}$$

$$T_{m\max} = K_{opt}\omega_{wopt}^2 \tag{3.7}$$

where K_{opt} is a constant determined by the characteristics of the wind turbine and given by the following equation:

$$K_{opt} = \frac{1}{2} C_p(\lambda, \beta)\rho\pi r^5 \tag{3.8}$$

3.3 Maximum Power Point Tracking

The electrical load of the generator in Fig. 3.1 should be regulated suitably for maximizing the active power extraction of a wind turbine at any given instant. It can be neither too large nor too small for a particular wind speed, otherwise the operating point of the wind turbine will deviate from the optimal power point and the efficiency of the wind turbine will be lower [16]. The wind turbine can only generate a maximum power for a particular wind speed and can acquire more power from the wind by decreasing or increasing the load on the generator via regulating the speed of the generator.

A lot of methods on the MPPT have been proposed. The simplest method is based on the tip speed of the wind turbine. Assume that the optimal value of the tip speed ratio can be obtained from Eq. (3.5), the optimal speed of the wind turbine can be calculated from Eq. (3.14) by:

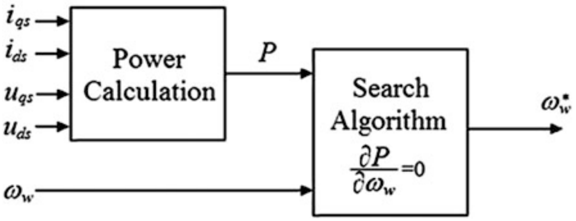

Fig. 3.2 the block diagram of the MPPT control system

$$\omega_{wopt} = \frac{\lambda_{opt}}{r} v_w \tag{3.9}$$

Although this method is simple, it needs an additional anemometer for measuring the wind speed in the tip of the wind turbine, which is much difficult.

Another more popular method for MPPT is based on the active power of the generator. Suppose that the generator in the wind turbine is an induction generator. The block diagram of the MPPT control system for the wind turbine is shown in Fig. 3.2.

For the induction generator, the active and reactive power can be expressed as follows, respectively:

$$P = i_{qs} u_{qs} + i_{ds} u_{ds} \tag{3.10}$$

$$Q = i_{qs} u_{qs} - i_{ds} u_{ds} \tag{3.11}$$

where i_{ds} and i_{qs} are the stator currents in d-q axes, u_{ds} and u_{qs} the stator voltages in d-q axes.

In Fig. 3.2, the search algorithm is basically based on the calculation of the power gradient to the speed of the wind turbine. Since the curve of the power versus the turbine speed is convex, there is no local maximum among the whole turbine speed. Hence based on the power gradient, the search algorithm can find the maximum point corresponding to the maximum power point of the wind turbine and finally produce the reference speed of the generator. To obtain maximum power from the wind, the speed of the wind turbine should be always controlled to rotate at the optimal speed $\omega_{\omega opt}$ by controlling the speed of the generator.

3.4 Model of Wind Energy Conversion System

The block diagram of the WECS is shown in Fig. 3.3. The back-to-back PWM converters are utilized in the WECS, and consist of the generator-side PWM converter, the intermediate DC circuit and the grid-side PWM converter. As shown in Fig. 3.3, the left is the distribution power networks, the right the generator,

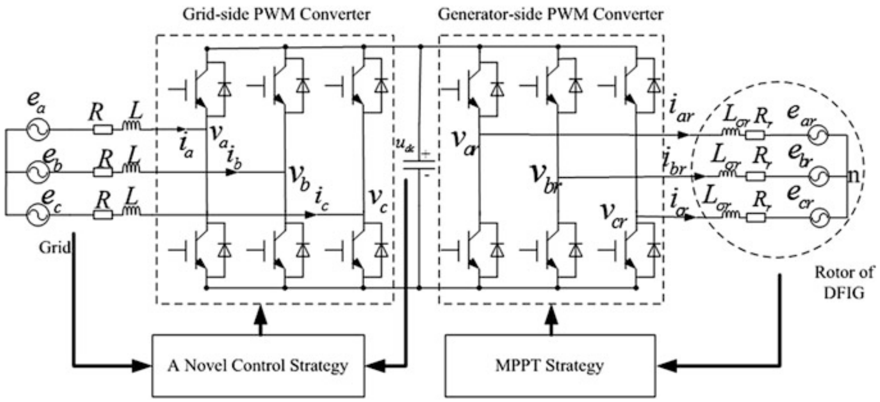

Fig. 3.3 Back-to-back PWM converter topology

which may be an induction generator, a permanent magnet synchronous generator, or a DFIG. The intermediate DC circuit makes it possible for the two sides to be controlled independently.

Back-to-back PWM converters have many significant advantages, such as unity power factor, bidirectional power flow, and controllable DC-link voltage [17], which makes it widely used in many industrial applications. To achieve these performances simultaneously, the design of controllers is important. At present, there are many researches on the design of the controllers. With the development of the design method, it can be roughly classified into two categories: linear and nonlinear control. In [18] and [19], proportional-integral (PI) controllers have been proposed, which are for achieving unity power factor, meanwhile a cascaded PI controller is used to regulate the DC-link voltage indirectly by controlling the input currents. However, the design of these controllers depends on the accurate parameters of the system to provide a linear model, so they are sensitive to parameter disturbances. Since the grid-side PWM converter is a multiple variables, strong coupling nonlinear system, the nonlinear control strategy without ignoring nonlinearities of the system can achieve better both static and dynamic performances. Nonlinear control methods, such as fuzzy control methods, are applied to improve the system performance [20, 21], which are lack of theoretical analysis and cannot ensure stability and damping characteristics of the closed-loop system.

Fig. 3.4 The Grid-side PWM Converter Model

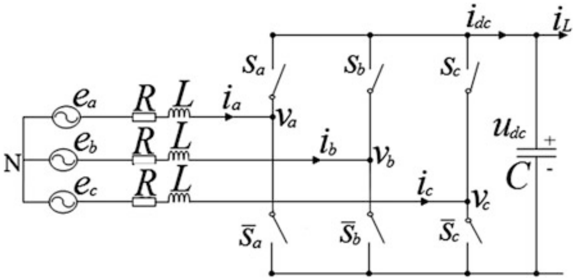

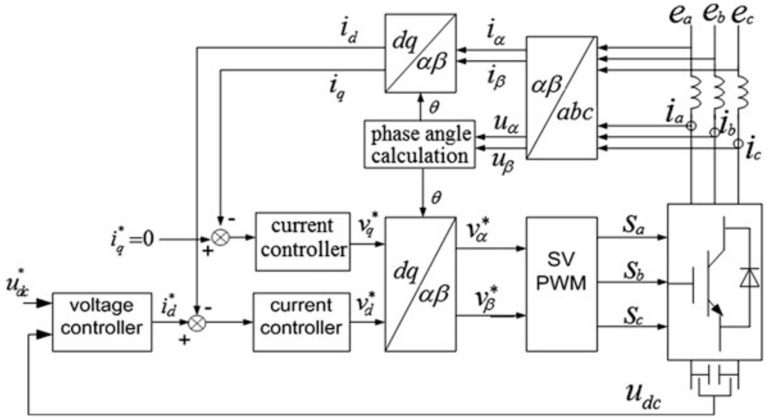

Fig. 3.5 Diagram of VOC scheme

Feedback linearization techniques [22, 23], which show an enhanced performance in simulation, however, are sensitive to model uncertainties. Hence sliding-mode control will be applied in the chapter.

The grid-side PWM converter model is shown in Fig. 3.4, where L is the inductor of the grid side filter, R the resistance, C the DC-link capacitor. The input line voltages and currents are expressed by the notations v_k and $i_k, k = a, b, c$.

In this chapter, the voltage-oriented control (VOC) scheme is used. It is a dual-loop structure including DC-link voltage outer loop and dq-axes current inner loop. A reference frame is chosen to rotate synchronously with the grid voltage space vector and the d-axis is made to orient to the grid voltage space vector. The block diagram of VOC is shown in Fig. 3.5. For converter, VOC can achieve decoupling between active and reactive currents as the d-axis of the synchronously rotating d-q frame is aligned with the grid voltage vector. The mathematical model in d-q synchronous rotating reference frame can be expressed by [16]

$$\begin{cases} L\dot{i}_d = -Ri_d + \omega Li_q + e_d - s_d u_{dc} \\ L\dot{i}_q = -Ri_q - \omega Li_d + e_q - s_q u_{dc} \\ C\dot{u}_{dc} = (s_d i_d + s_q i_q) - i_L \end{cases} \tag{3.12}$$

where i_d, i_q are the d- and q-axis current components of the converter; s_d, s_q the d- and q-axis switching control signals in d-q reference frame; e_d and e_q the d- and q-axis voltage component of the three-phase supply; ω the angular frequency of the power source.

It can be seen from Eq. (3.12) that it is difficult to design the regulators due to the multiplication of the state variables by the control inputs. To design the controllers, the dynamical Eq. (3.12) should be simplified based on the power balance between AC and DC sides of the system. The active power of AC and DC sides are expressed by the notations P_{ac} and P_{dc} respectively. Neglecting the converter loss, the active power of the AC side is equal to the active power of the DC side, i.e.,

$$P_{ac} = P_{dc} \tag{3.13}$$

The active power of AC and DC sides can be calculated by:

$$P_{ac} = e_d i_d + e_q i_q \tag{3.14}$$

$$P_{dc} = u_{dc} i_{dc} = u_{dc}(C\dot{u}_{dc} + i_L) \tag{3.15}$$

Based on Eqs. (3.13)–(3.15), it can be obtained:

$$u_{dc}(C\dot{u}_{dc} + i_L) = e_d i_d + e_q i_q \tag{3.16}$$

Define a new variable $u = u_{dc}^2$. Equation (3.16) can be simplified as:

$$\dot{u} = \frac{2}{C}(e_d i_d + e_q i_q) - \frac{2}{C}\sqrt{u} i_L \tag{3.17}$$

Now from Eqs. (3.12) and (3.17), new dynamic model of the converter in *d*-*q* synchronous rotating reference frame can be expressed as:

$$\begin{cases} L\dot{i}_d = -Ri_d + \omega L i_q + e_d - u_d \\ L\dot{i}_q = -Ri_q - \omega L i_d + e_q - u_q \\ \dot{u} = \frac{2}{C}(e_d i_d + e_q i_q) - \frac{2}{C}\sqrt{u} i_L \end{cases} \tag{3.18}$$

where $u_d = s_d \cdot u_{dc}$, $u_q = s_q \cdot u_{dc}$.

As the *d*-axis of the synchronously rotating *d*-*q* frame is aligned with the grid voltage vector, *d*- and *q*-axis components of grid voltage can be obtained as follows:

$$\begin{cases} e_d = E_s \\ e_q = 0 \end{cases} \tag{3.19}$$

where E_s is equal to the grid voltage vector. So Eq. (3.18) can be further simplified as:

$$\begin{cases} L\dot{i}_d = -Ri_d + \omega L i_q + E_s - u_d \\ L\dot{i}_q = -Ri_q - \omega L i_d - u_q \\ \dot{u} = \frac{2}{C} E_s i_d - \frac{2}{C}\sqrt{u} i_L \end{cases} \tag{3.20}$$

It can be seen from Eq. (3.20) that the DC-link voltage, $u_{dc} = \sqrt{u}$, can be controlled using the q-axis current, i_d.

3.5 Control Strategy for Wind Energy Integration into Power Network

In the WECS, as shown in Fig. 3.3, the energy generated by a generator is firstly transformed to a DC voltage by the machine side PWM inverter connecting the machine to the DC link. Then, the grid side PWM inverter connecting the DC link to the power grid transforms the DC to AC voltages, which is delivered to the power grid. We can use the dual PWM inverters to transform the renewable energy to the grid without any additional circuit. The machine side PWM inverter and the grid side PWM inverter are independent. Both of them can be controlled separately. A unit power ratio for the WECS can be realized using some control strategy.

It can be seen in Fig. 3.3 that the output of the DC-link voltage controller is the d-axis reference current i_d^*. For achieving the rectification or the inversion with unity power factor, the component of the reactive current i_q^* should be set to zero [24].

3.5.1 DC-Link Voltage Controller Design

Define the given DC-link voltage as u_{dc}^* and its square as $u^* = u_{dc}^{*2}$, then the error between the square of the DC-link and the square of the given DC-link voltage e_1 is:

$$e_1 = u^* - u \tag{3.21}$$

Based on Eq. (3.20), the error e_1 can be expressed as:

$$\dot{e}_1 = \dot{u}^* - \dot{u} = -\frac{2}{C} E_s i_d + \frac{2}{C}\sqrt{u} i_L \tag{3.22}$$

To achieve fast error convergence and better tracking precision, a TSM manifold was designed as follows [12, 13]:

$$s_1 = \dot{e}_1 + \gamma_1 e_1^{q_1/p_1} \tag{3.23}$$

where $\gamma_1 > 0$, $p_1 > 0$, $q_1 > 0$, p_1 and q_1 are odd.

After the system states reach the TSM manifold $s_1 = 0$ in finite time, both e_1 and $\dot{e}_1$ will converge to the original points along $s_1 = 0$ in finite time, i.e.,

$$e_1 = \dot{e}_1 = 0 \tag{3.24}$$

Theorem 1 *If the TSM manifold is chosen as Eq.* (3.23), *and the TSM control is designed as follows*, e_1 *can converge to zero in finite time* [25]:

$$i_d^* = i_{deq}^* + i_{dn}^* \tag{3.25}$$

$$i_{deq}^* = \frac{\sqrt{u}}{E_s} i_L + \frac{C}{2E_s} \gamma_1 e_1^{q_1/p_1} \tag{3.26}$$

$$\dot{i}_{dn}^* + T_1 i_{dn}^* = v \tag{3.27}$$

$$v = (k_1 + \eta_1)\mathrm{sgn}(s_1) \tag{3.28}$$

where $\eta_1 = \max(|T_1 i_{dn}^*|),\ T_1 > 0,\ k_1 > 0.$

Proof Consider the following Lyapunov function:

$$V = \frac{1}{2} s_1^2 \tag{3.29}$$

Differentiating V with respect to time gives:

$$\dot{V} = s_1 \dot{s}_1 \tag{3.30}$$

Based on Eqs. (3.22) and (3.23), it can be obtained:

$$s_1 = -\frac{2}{C} E_s i_d + \frac{2}{C} \sqrt{u} i_L + \gamma_1 e_1^{q_1/p_1}$$

Substituting Eqs. (3.25) and (3.26) into the above equation gives:

$$s_1 = -\frac{2}{C} E_s i_{dn}^*$$

Differentiating s_1 with respect to time, it can be obtained:

$$\dot{s}_1 = -\frac{2}{C} E_s \dot{i}_{dn}^*$$

Substituting the above equation into Eq. (3.30) gives:

$$s_1 \dot{s}_1 = -\frac{2}{C} E_s s_1 \dot{i}_{dn}^*$$

Substituting Eqs. (3.27) and (3.28) into the above equation gives:

$$\begin{aligned} s_1\dot{s}_1 &= -\frac{2}{C}E_s s_1 \dot{i}^*_{dn} \\ &= -\frac{2}{C}E_s s_1(\dot{i}^*_{dn} + T_1 i^*_{dn} - T_1 i^*_{dn}) \\ &= -\frac{2}{C}E_s s_1((k_1+\eta_1)\mathrm{sgn}(s_1) - T_1 i^*_{dn}) \\ &= -\frac{2}{C}E_s((k_1+\eta_1)|s_1| - T_1 s_1 i^*_{dn}) \\ &\leq -\frac{2}{C}E_s k_1 |s_1| \end{aligned}$$

i.e.,

$$\dot{V}_1 \leq -\frac{2}{C}E_s k_1 |s_1| < 0 \text{ for } |s_1| \neq 0$$

The system (3.22) satisfies the sufficient condition of the existence of the sliding mode. Therefore, the states of the system (3.22) can reach the TSM manifold $s_1 = 0$ within finite time.

3.5.2 d-*Axis Current Controller Design*

Define an error variable between the required and actual *d*-axis current:

$$e_2 = i_d^* - i_d \tag{3.31}$$

Based on Eq. (3.20), the *d*-axis current error dynamics can be expressed by:

$$\dot{e}_2 = \dot{i}_d^* + \frac{R}{L}i_d - \omega i_q - \frac{E_s}{L} + \frac{u_d}{L} \tag{3.32}$$

A TSM manifold is designed as follows [12, 13]:

$$s_2 = \dot{e}_2 + \gamma_2 e_2^{q_2/p_2} \tag{3.33}$$

where $\gamma_2 > 0$, $p_2 > 0$, $q_2 > 0$, p_{22} and q are odd.

Theorem 2 *If the TSM manifold is chosen as Eq.* (3.33), *and the control is designed as follows*, e_2 *can converge to zero in finite time* [25]:

$$u_d = u_{deq} + u_{dn} \tag{3.34}$$

$$u_{deq} = -L\dot{i}_d^* - Ri_d + \omega L i_q + E_s - L\gamma_2 e_2^{q_2/p_2} \tag{3.35}$$

$$\dot{u}_{dn} + T_2 u_{dn} = v \tag{3.36}$$

$$v = -(k_2 + \eta_2)\mathrm{sgn}(s_2) \tag{3.37}$$

where $\eta_2 = \max(|T_2 u_{dn}|),\ T_2 > 0,\ k_2 > 0.$

3.5.3 q-*Axis Current Controller Design*

Define an error variable between the required and actual q-axis current:

$$e_3 = i_q^* - i_q \tag{3.38}$$

Based on Eq. (3.20), the q-axis current error dynamics can be expressed by:

$$\dot{e}_3 = \frac{R}{L} i_q + \omega i_d + \frac{u_q}{L} \tag{3.39}$$

A TSM manifold is designed as follows [12, 13]:

$$s_3 = \dot{e}_3 + \gamma_3 e_3^{q_3/p_3} \tag{3.40}$$

where $\gamma_3 > 0$, $p_3 > 0$, $q_3 > 0$, p_3 and q_3 are odd.

Theorem 3 *If the TSM manifold is chosen as Eq.* (3.40), *and the control is designed as follows*, e_3 *can converge to zero in finite time* [25]:

$$u_q = u_{qeq} + u_{qn} \tag{3.41}$$

$$u_{qeq} = -Ri_q - \omega L i_d - L\gamma_3 e_3^{q_3/p_3} \tag{3.42}$$

$$\dot{u}_{qn} + T_3 u_{qn} = v \tag{3.43}$$

$$v = -(k_3 + \eta_3)\mathrm{sgn}(s_3) \tag{3.44}$$

where $\eta_3 = \max(\left|T_3 u_{qn}\right|),\ T_3 > 0,\ k_3 > 0.$

The proof of Theorems 2 and 3 is similar to that of Theorem 1 and hence is omitted here.

In Theorem 2 and 3, the control signals, u_d and u_q, can be transformed to the control signals s_d and s_q in Eq. (3.12) by using the following equations:

Fig. 3.6 u_{dc} in load current change

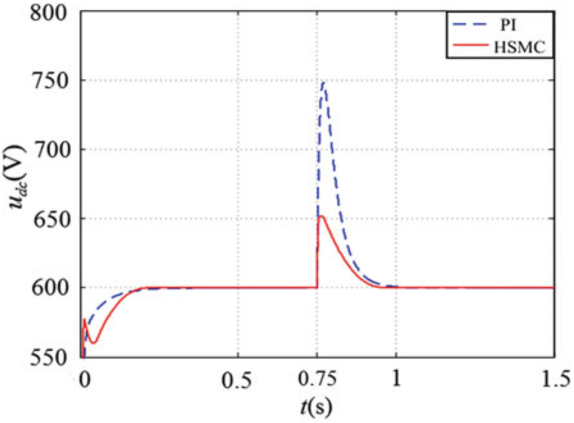

Fig. 3.7 e_a and i_a in load current change

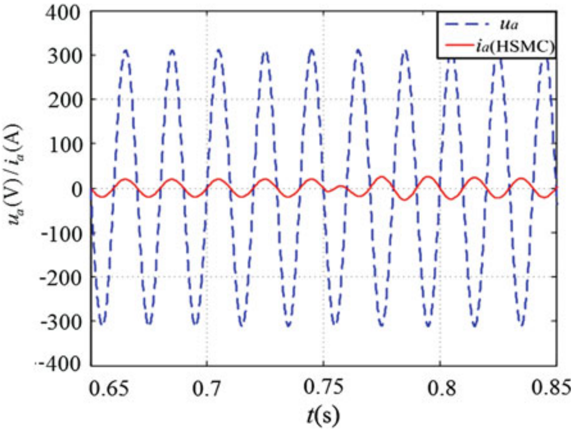

$$s_d = u_d / u_{dc} \tag{3.45a}$$

$$s_q = u_q / u_{dc} \tag{3.45b}$$

3.6 Simulations

The parameters of the gird-side PWM converter are given as follows [25]:

$E_m = 220\sqrt{2}$(V), $L = 0.006$(H), $R = 0.5(\Omega)$, $C = 0.00136$(F), $u_{dc}^* = 600$(V), $f = 50$ (HZ).

To prove the validity and advantages of the new control strategy, the results are compared between the high-order TSM control strategy and the traditional PI control strategy. In order to illustrate the fast error convergence and strong robustness of the new control strategy, the results under different cases are given, such as step changes in the load currents and step changes in the source voltages.

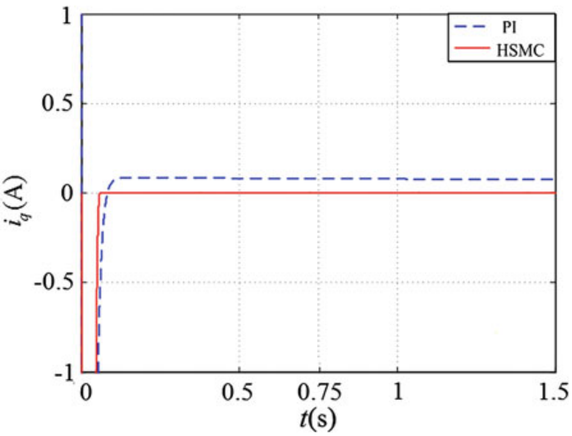

Fig. 3.8 i_q in load current change

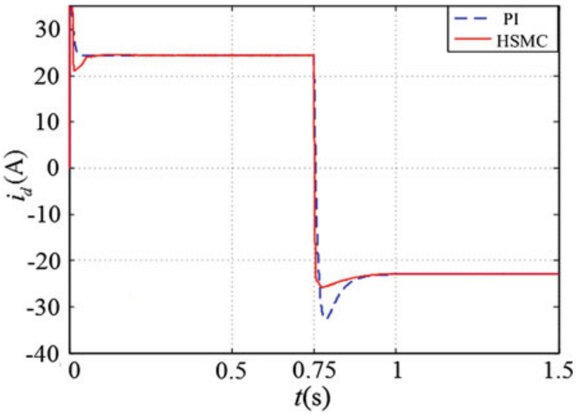

Fig. 3.9 i_d in load current change

3.6.1 Step Changes in the Load Current

In this test, the load current is changed from 15A to -15A at the time $t = 0.75$ s. It can be seen from Fig. 3.6 that the DC-link voltage with the TSM control can track the given voltage and have lower ripple and faster convergence than that using PI control. From Fig. 3.7, it can be seen that the grid-side PWM converter works as a rectifier with unity power factor and absorbs the energy from the power grid before $t = 0.75$ s and works as an inverter with unity power factor and transfer the energy to the power grid after $t = 0.75$ s. Figure 3.8 shows that the current in q-axis converges to zero, and the TSM control has higher tracking accuracy. Figure 3.9 presents that the error of the current in d-axis with the TSM control strategy can achieve lower ripples and faster convergence. The control signals for SMC and TSMC control are shown in Figs. 3.10 and 3.11. It can be seen that traditional SMC signals exist chattering, but high-order TSM control signals are smooth.

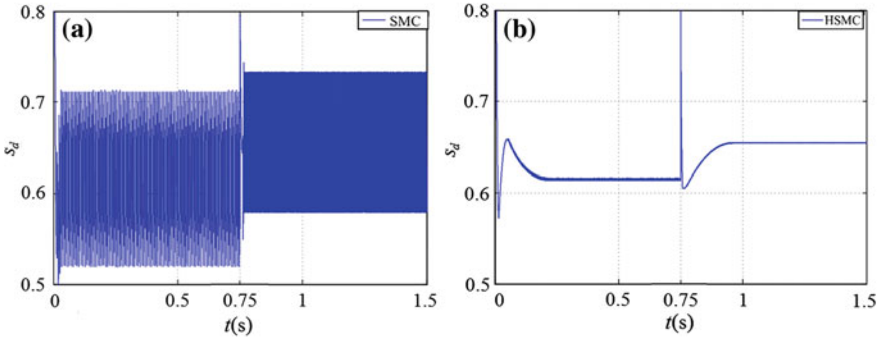

Fig. 3.10 Control signals in *d*-axis. **a** traditional SMC; **b** high-order TSMC

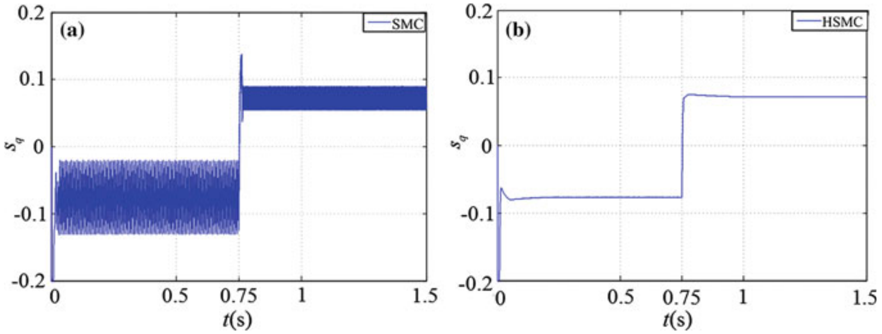

Fig. 3.11 Control signals in *q*-axis. **a** traditional SMC; **b** high-order TSMC

Fig. 3.12 u_{dc} in the source voltage change

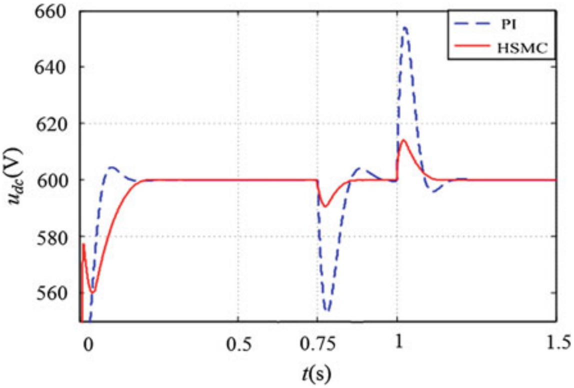

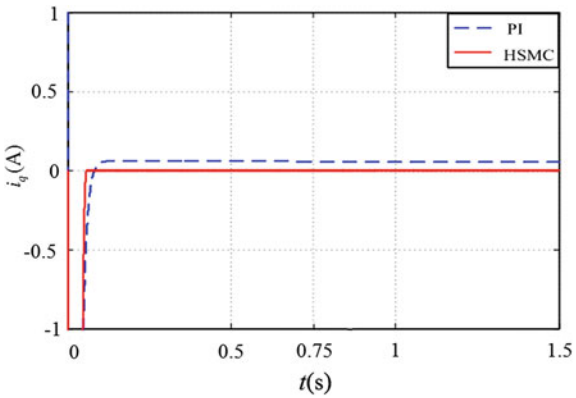

Fig. 3.13 i_q in the source voltage change

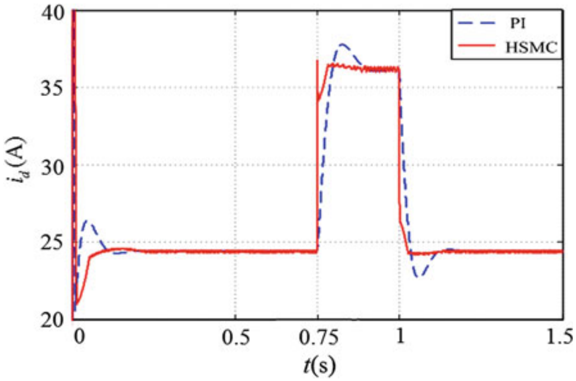

Fig. 3.14 i_d in the source voltage change

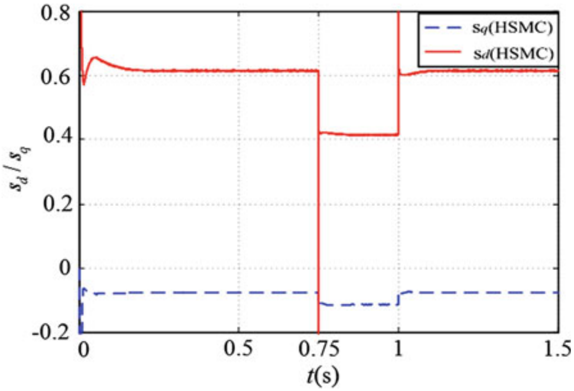

Fig. 3.15 Control signals of the inverter

3.6.2 Step Changes in the Source Voltage

The amplitude of source voltage reduces by 20 % at 0.75 s and restores to initial value at 0.85 s. The load current is 15 A. The DC-link voltage responses to step changes of the voltage in the power grid in Fig. 3.12. It can be seen that the DC-link voltage almost has no fluctuations when the system is controlled by high-order TSM control. The *q*- and *d*-axis current responses to step changes in source voltage are depicted in Figs. 3.13 and 3.14. The control signals of the inverter are displayed in Fig. 3.15.

3.7 Conclusions

This chapter has described the control issues in grid integration of WECS. A structure of dual PWM inverter is presented in the wind energy integration into power network. Both of two PWM inverters are controlled separately using one control system. A control strategy for the grid-side PWM inverter has been designed to guarantee that the WECS has a unit power ratio. Sliding-mode control theory and technique have been used to optimize the control of WECS. A control strategy for the grid-side PWM converter of DFIG-based wind power system has been developed. The high-order TSM control technique provides the fast convergence, strong robustness, and high tracking accuracy. A smooth control signal of the controller can be generated by utilizing the second-order sliding-mode technique. The effect of the equivalent low pass filter in the high-order sliding-mode mechanism can be regulated optionally. The simulation results have shown the correctness of the proposed method.

Although a lot of theoretical research work on the control of WECS has been done, the future work will involve providing more efficient and robust control algorithms, and trying to do experiments in practical application environments.

Acknowledgments This work was supported in part by the National Natural Science Foundation of China (61074015), and also in part by ARC Linkage Project (LP100200538) of the Australian Research Council.

References

1. REN21 (2011) Renewables 2011: Global Status Report. http://www.ren21.net/Portals/97/documents/GSR/GSR2011_Master18.pdf
2. The Encyclopedia (2011) wind energy conversion system. http://www.daviddarling.info/encyclopedia/W/AE_wind_energy_conversion_system.html
3. Thongam JS, Bouchard P, Beguenane R, Fofana I (2010) Neural network based wind speed sensorless MPPT controller for variable-speed wind energy conversion systems. In: Proceedings of IEEE electric power energy conference: "sustainable energy intelligent grid", Halifax, NS, USA, 25–27 Aug 2010
4. De Battista H, Mantz RJ, Christiansen CF (2000) Dynamical sliding mode power control of wind driven induction generators. IEEE Trans Energy Convers 15(4):451–457

5. Susperregui A, Tapia G, Martinez MI, Blanco A (2011) Second-order sliding-mode controller design and tuning for grid synchronization and power control of a wind turbine-driven DFIG. In: Proceedings of the IET conference on renewable power generation (RPG 2011), Edinburgh, UK, 6–8 Sept 2011
6. Hasanien HM, Muyeen SM (2012) Speed control of grid-connected switched reluctance generator driven by variable speed wind turbine using adaptive neural network controller. Electr Power Syst Res 84(1):206–213
7. Yu X, Man Z (1996) Model reference adaptive control systems with terminal sliding modes. Int J Control 64(6):1165–1176
8. Feng Y, Zheng J, Yu X, Truong NV (2009) Hybrid terminal sliding-mode observer design method for a permanent-magnet synchronous motor control system. IEEE Trans Ind Electron 56(9):3424–3431
9. Feng Y, Yu X, Han F (2013) On nonsingular terminal sliding-mode control of nonlinear systems. Automatica 49(6):1715–1722
10. Feng Y, Han X, Wang Y, Yu X (2007) Second-order terminal sliding mode control of uncertain multivariable systems. Int J Control 80(6):856–862
11. Feng Y, Bao S, Yu X (2004) Inverse dynamics nonsingular terminal sliding mode control of two-link flexible manipulators. Int J Robot Autom 19(2):91–102
12. Feng Y, Yu XH, Man ZH (2002) Nonsingular adaptive terminal sliding mode control of rigid manipulators. Automatica 38(12):2167–2179
13. Feng Y, Yu X, Han F (2013) High-order terminal sliding-mode observer for parameter estimation of a permanent magnet synchronous motor. IEEE Trans Ind Electron 60(10):4272–4280
14. Anderson PM, Bose A (1983) Stability simulation of wind turbine systems. IEEE Power Appar Syst PAS-102(12):3791–3795
15. Ghanes M, Zheng G (2009) On sensorless induction motor drives: sliding-mode observer and output feedback controller. IEEE Trans Ind Electron 56(9): 3404–3413
16. Feng Y, Zhou M, Wang Y, Yang Y (2013) High-order terminal sliding-mode control strategy for wind energy Integration into power network. In: Proceedings of the 32nd chinese control conference (CCC), Xi'an, China, 26–28 Jul 2013, pp 3186–3189
17. Malesani L, Rossetto L, Tomasin P (1993) AC/DC/AC PWM Converter with Minimum Energy Storage in the DC Link. In: Proceedings of IEEE applied power electronics conference APEC'93, San Diego, CA, USA, 7–11 Mar 1993, pp 306–311
18. Blasko V, Kaura V (1997) A new mathematical model and control of three-phase AC-DC voltage source converter. IEEE Trans Power Electron 12(1):116–123
19. Green AW, Boys JT (1989) Hysteresis current-forced three-phase voltage-sourced reversible rectifier. IEEE Trans Power Electron 136(3):113–120
20. Kazmierkowski MP, Cichowlas M, Jasinski M (2003) Artificial intelligence based controllers for industrial PWM power converters. In: Proceedings of the IEEE international conference industrial informatics, Banff, Alta., Canada, 21–24 Aug 2003, pp 187–191
21. Konstantopoulos GC (2012) "Novel dynamic nonlinear control scheme for three-phase AC/DC voltage source converters. In: Proceedings of 2012 IEEE international conference industrial technology, ICIT 2012, Athens, Greece, 19–21 Mar 2012, pp 638–643
22. Lee TS (2003) Input-output linearization and zero-dynamics control of three-phase AC/DC voltage-source converters. IEEE Trans Power Electron 18:11–22
23. Deng WH, Hu ZB (2005) "The research of decoupled state variable feedback linearization control method of three-phase voltage source PWM rectifier. Proc CSEE (China) 25(7):97–103
24. Komurcugil H, Kukrer O (2005) A novel current-control method for three-phase PWM AC/DC voltage-source converters. IEEE Trans Ind Electron 46(3):544–553
25. Chen B, Feng Y, Zhou M (2013) Terminal sliding-mode control scheme for grid-side PWM converter of DFIG-based wind power system. In: Proceedings of 39th annual conference of the IEEE industrial electronics society (IECON 2013), Vienna, Austria, 10-13 Nov 2013, pp 8014–8018